



**HAL**  
open science

## Chemical Activity of the Peroxide/Oxide Redox Couple: Case Study of Ba<sub>5</sub>Ru<sub>2</sub>O<sub>11</sub> in Aqueous and Organic Solvents

Alexis Grimaud, Antonella Iadecola, Dmitry Batuk, Matthieu Saubanère,  
Artem Abakumov, John William Freeland, Jordi Cabana, Haifeng Li,  
Marie-Liesse Doublet, Gwenaëlle Rousse, et al.

### ► To cite this version:

Alexis Grimaud, Antonella Iadecola, Dmitry Batuk, Matthieu Saubanère, Artem Abakumov, et al.. Chemical Activity of the Peroxide/Oxide Redox Couple: Case Study of Ba<sub>5</sub>Ru<sub>2</sub>O<sub>11</sub> in Aqueous and Organic Solvents. Chemistry of Materials, 2018, 30 (11), pp.3882-3893. 10.1021/acs.chemmater.8b01372 . hal-02388363

**HAL Id: hal-02388363**

**<https://hal.science/hal-02388363>**

Submitted on 1 Dec 2019

**HAL** is a multi-disciplinary open access archive for the deposit and dissemination of scientific research documents, whether they are published or not. The documents may come from teaching and research institutions in France or abroad, or from public or private research centers.

L'archive ouverte pluridisciplinaire **HAL**, est destinée au dépôt et à la diffusion de documents scientifiques de niveau recherche, publiés ou non, émanant des établissements d'enseignement et de recherche français ou étrangers, des laboratoires publics ou privés.

# On the chemical activity of the peroxide/oxide redox couple: case study of $\text{Ba}_5\text{Ru}_2\text{O}_{11}$ in aqueous and organic solvents

Alexis Grimaud,<sup>1,2\*</sup> Antonella Iadecola,<sup>2</sup> Dmitry Batuk,<sup>1,3</sup> Matthieu Saubanère,<sup>2,4</sup> Artem M.

Abakumov,<sup>3</sup> John W. Freeland,<sup>5</sup> Jordi Cabana,<sup>6,7</sup> Haifeng, Li,<sup>6</sup> Marie-Liesse Doublet,<sup>2,4</sup>

Gwenaëlle Rousse<sup>1,2,8</sup> and Jean-Marie Tarascon<sup>1,2,8,9</sup>.

1 - Chimie du Solide et de l'Énergie, UMR 8260, Collège de France, 75231, Paris Cedex 05, France

2 - Réseau sur le Stockage Electrochimique de l'Énergie (RS2E), CNRS FR 3459, 33 rue Saint Leu, 80039, Amiens Cedex, France

3 - EMAT, University of Antwerp, Groenenborgerlaan 171, 2020, Belgium

4 - Institut Charles Gerhardt, CNRS UMR 5253, Université Montpellier, Place E. Bataillon, 34095 Montpellier, France

5 - Advanced Photon Source, Argonne National Laboratory, Argonne, IL 60439, USA

6 - Department of Chemistry, University of Illinois at Chicago, Chicago, Illinois 60607, United States

7 - Joint Center for Energy Storage Research (JCESR), Argonne National Laboratory, Lemont, Illinois 60439, United States

8 - Sorbonne Universités - UPMC Université Paris 06, Paris, France

9 - ALISTORE-European Research Institute, Amiens, France

Corresponding Author:

\* E-mails: [alexis.grimaud@college-de-france.fr](mailto:alexis.grimaud@college-de-france.fr)

**Abstract:**

The finding that triggering the redox activity of oxygen ions within the lattice of transition metal oxides can boost the performances of materials used in energy storage and conversion devices such as Li-ion batteries or oxygen evolution electrocatalysts has recently spurred intensive and innovative researches in the field of energy. While experimental and theoretical efforts have been critical to understand the role of oxygen non-bonding states in the redox activity of oxygen ions, a clear picture of the redox chemistry of the oxygen species formed upon this oxidation process is still missing. This can be, in part, explained by the complexity in stabilizing and studying these species once electrochemically formed. In this work, we alleviate this difficulty by studying the phase  $\text{Ba}_5\text{Ru}_2\text{O}_{11}$  - which contains peroxide  $\text{O}_2^{2-}$  groups - as oxygen evolution reaction electrocatalyst and Li-ion battery material. Combining physical characterization and electrochemical measurements, we demonstrate that peroxide groups can easily be oxidized at relatively low potential, leading to the formation of gaseous dioxygen and to the instability of the oxide. Furthermore, we demonstrate that, owing to the stabilization at high energy of peroxide, the high-lying energy of the empty  $\sigma^*$  antibonding O-O states limits the reversibility of the electrochemical reactions when the  $\text{O}_2^{2-}/\text{O}^{2-}$  redox couple is used as redox center for Li-ion battery materials or as OER redox active sites is foreseen. Overall, this work suggests that the formation of true peroxide  $\text{O}_2^{2-}$  states are detrimental for transition metal oxides used as OER catalysts and Li-ion battery materials. Rather, oxygen species with O-O bond order lower than 1 would be preferred for these applications.

## Introduction

The deployment of renewable energies is arguably one of the major challenges faced by humankind, which will only be achieved by the development of efficient energy storage and conversion devices. Electrochemical devices such as batteries, supercapacitors or electrolyzers will certainly take a major role, provided that cost-effective and earth abundant materials can be developed in order to master the complex electrochemical reactions happening at the electrodes.<sup>1-3</sup> The fields of batteries and electrocatalysis were so far regarded as antagonists since the former is governed by bulk processes while the latter is controlled by kinetics on the surface of materials. Nevertheless, they recently became closer, owing to the realization that mastering the redox chemistry of oxygen ions is at the heart of the development of both energy-dense Li-rich layered compounds for Li-ion batteries and better oxygen evolution reaction (OER) catalysts.<sup>4-8</sup>

The quest for mastering the redox chemistry of oxide ions in transition metal oxides has significantly advanced the understanding of the field (Figure 1). For Li-rich layered compounds, theoretical and experimental reports pointed towards the importance of accessing the energy level of non-bonding 2p oxygen states. Upon oxidation, lattice oxygen ions  $O^{2-}$  can form O-O bonds and the so-called peroxo-like species  $(O_2)^{n-}$  that are characterized by relatively short O-O distances with a low bond order (lower than 1) and the formation of new energy states close to the Fermi level.<sup>5,9-13</sup> This reversible process occurs at potential lower than about 4.3 V vs.  $Li^+/Li$ . When pushing above this potential, which corresponds to the standard potential  $E^\circ(O_2/H_2O)$  at pH = 0, the direct four electron formation of gaseous oxygen can occur through the condensation of O-O states within the lattice of the transition metal oxide. The correspondence between both phenomena can be

rationalized assuming a similar chemical potential of oxide ions in the bulk of the transition metal oxide and in water (a similar assumption is made when considering the chemical potential of lithium inside the insertion electrode and in metallic lithium which is used as reference in thermodynamic calculations). This similarity is further exemplified when noting that bulk oxygen release was observed for  $\text{Mn}^{4+}$ -based  $\text{Li}_2\text{MnO}_3$ .<sup>9,14,15</sup> Indeed, for both  $\text{Mn}^{4+}$ -based oxygen evolving center (OEC),<sup>16</sup> cofactor of the Photosystem II (PSII) which naturally oxidizes water to evolve oxygen, and  $\text{Li}_2\text{MnO}_3$  no  $\text{Mn}^{5+}$  was observed upon oxidation. Rather, for the OEC the oxidation of water occurs through the formation of oxidized oxygen radicals.<sup>17</sup> More striking is the similar O-O bond distance of about 2.1 - 2.4 Å found for these Mn-based oxides upon oxidation and the oxyl-oxo bond formation for the cofactor.<sup>18-20</sup> Besides, similar O-O bond formation occurs for Ru-based compounds used as homogeneous OER catalysts and Li-ion battery materials.<sup>5,21</sup> This relatively large O-O bond distance indicates a low bond order and the formation of a peroxy-like  $(\text{O}_2)^{n-}$  species with n being close to 3 upon one electron removal, rather than “true” peroxide  $(\text{O}_2)^{2-}$  species.

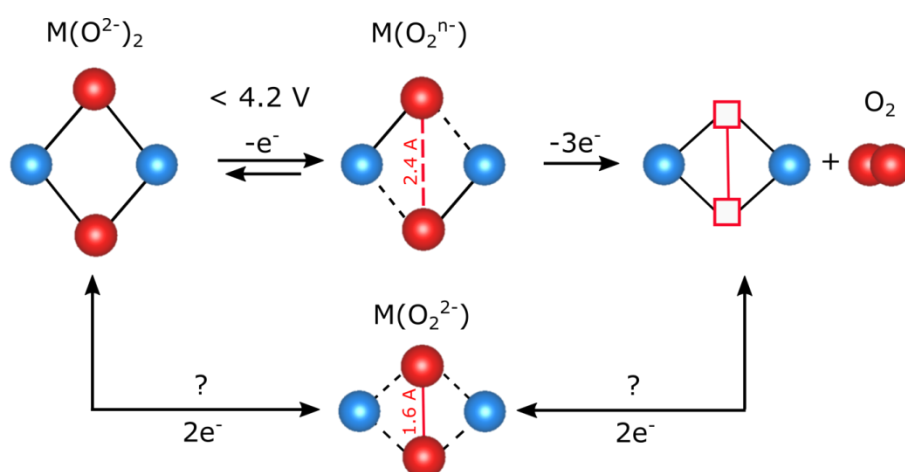


**Figure 1:** Schematic representation of the oxygen redox chemistry in transition metal oxides with the transition from oxide ion ( $\text{O}^{2-}$ ) to peroxy-like  $(\text{O}_2)^{n-}$  groups, peroxide  $(\text{O}_2)^{2-}$  all the way to gaseous oxygen release.

Overall, a central question for mastering the redox activity of oxygen for the fields of batteries and electrocatalysts concerns the O-O bond formation that can either occur through the coupling of two lattice oxygen ions (mechanism poised as direct-coupling by the electrocatalysis community) or through the reaction of one oxidized oxygen ions (also called oxyl radical) with water or carbonate solvent molecules acting as nucleophilic species (mechanism defined as acid-base).<sup>22,23</sup> Evidences for both mechanisms were found for layered compounds used as Li-ion battery electrodes<sup>5,24-28</sup> as well as for transition metal oxides used as heterogeneous OER catalysts,<sup>29-34</sup> while the Mn-based cofactor of PSII is believed to evolve oxygen through a direct-coupling mechanism.<sup>19</sup> Nevertheless, questions still remain about the exact chemical and electronic nature of these O-O bonds and the stability of these intermediate species towards condensation and oxygen release. Hence, only a full understanding of them will allow for the development of better battery materials as well as catalysts for the OER.

Driven by these questions, we decided to study the redox behavior of O-O bonds in the bulk of transition metal oxides, but only a very few oxides were reported so far to contain true peroxide groups. Among them is the family of hexagonal perovskites with the compounds  $\text{La}_{1.2}\text{Sr}_{2.7}\text{MO}_{7.33}$ ,  $\text{La}_2\text{Sr}_2\text{PtO}_{7+\delta}$  or  $\text{Ba}_5\text{Ru}_2\text{O}_{11}$ .<sup>35-37</sup> In this work, we selected  $\text{Ba}_5\text{Ru}_2\text{O}_{11}$  as a model compound owing to its similarities with the well-studied Ru-based oxides used as battery electrode materials and OER catalysts. More specifically, we studied the redox chemistry of bulk peroxide groups pertaining to  $\text{Ba}_5\text{Ru}_2\text{O}_{11}$  by combining a physical and an electrochemical study in both aqueous and aprotic media.

## Results and discussions

The structure of the hexagonal perovskite  $\text{Ba}_5\text{Ru}_2\text{O}_{11}$  was previously reported by Darriet et al.<sup>37</sup> It is built on the alternating stacking of three  $\text{BaO}_3$  and one  $\text{Ba}_2\text{O}_2$  layers, where Ru occupies octahedral sites forming face-sharing  $\text{Ru}_2\text{O}_9$  dimers along [001] (Fig. 2a). The peroxide groups  $\text{O}_2^{2-}$  are located in the  $\text{Ba}_2\text{O}_2$  layers and are statistically distributed among three possible configurations due to the thermal entropy (Fig. 2b). The structure of a reduced phase (e.g; oxygen deficient)  $\text{Ba}_5\text{Ru}_2\text{O}_{10}$  shows the same symmetry and similar Ba-Ru framework as the parent compound,<sup>38</sup> in which the  $(\text{O}_2)^{2-}$  peroxide species are replaced by a single oxygen atom located at the origin of the cell (Fig. 2c). Therefore, we first confirmed that our sample is phase pure, by means of laboratory X-ray diffraction (XRD). The XRD pattern can be indexed using the  $P 6_3/m m c$  hexagonal space group with lattice parameters  $a = 5.95144(9) \text{ \AA}$  and  $c = 18.0537(3) \text{ \AA}$ . These lattice parameters are in line with those reported for  $\text{Ba}_5\text{Ru}_2\text{O}_{11}$  and expected to be larger than those for  $\text{Ba}_5\text{Ru}_2\text{O}_{10}$ . However, the use of XRD does not allow distinguishing between the  $\text{Ba}_5\text{Ru}_2\text{O}_{10}$  and the  $\text{Ba}_5\text{Ru}_2\text{O}_{11}$  structures as refinements performed with both structural models give equally good results. Therefore, the structure was refined using neutron powder diffraction (NPD), which is much more sensitive to oxygen than X-rays. The NPD patterns collected at two different wavelengths ( $\lambda = 1.29 \text{ \AA}$  and  $2.53 \text{ \AA}$ ) were simultaneously refined by the Rietveld method, using either the  $\text{Ba}_5\text{Ru}_2\text{O}_{10}$  structural model where one oxygen fully occupies the  $2a$  (0,0,0) position, or the  $\text{Ba}_5\text{Ru}_2\text{O}_{11}$  model, in which the  $2a$  oxygen is displaced to the  $12k$  ( $x, 2x, z$ ) position with a partial occupancy of 1/3, so as to form peroxide  $(\text{O}_2)^{2-}$  groups statistically distributed around the  $c$ -axis (Fig. 2b). The fit using the  $\text{Ba}_5\text{Ru}_2\text{O}_{10}$  model results in wrong relative intensities for the (004)/(102) doublet and leads to an unrealistic thermal parameter  $B_{\text{iso}}$  of  $15 \text{ \AA}^2$  for the oxygen atom in  $2a$  position (Fig. 3a and Table 1). In contrary, the

refinement using the  $\text{Ba}_5\text{Ru}_2\text{O}_{11}$  model gives a very good fit as seen in Fig. 3b, confirming the formation of peroxide ( $\text{O}_2$ )<sup>2-</sup> groups within the lattice of  $\text{Ba}_5\text{Ru}_2\text{O}_{11}$ . The final atomic positions are reported in Table 1 giving the O-O bond length of 1.617 Å for the peroxide groups.

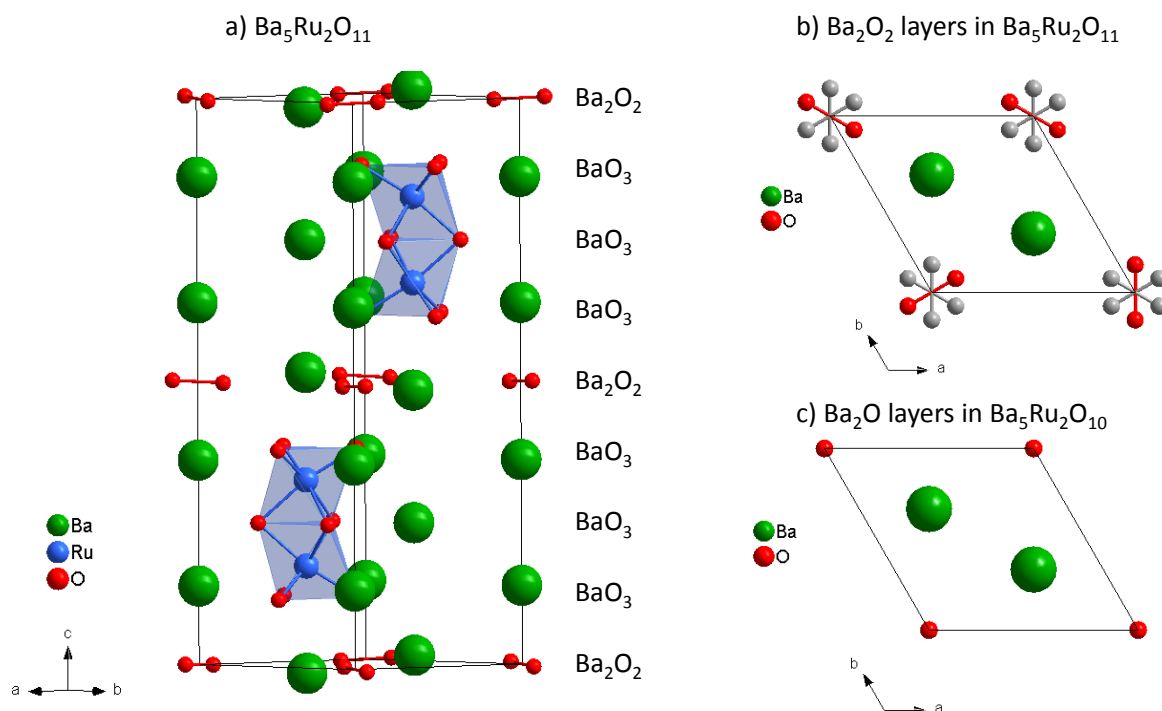


**Figure 2:** **a.** Structure of  $\text{Ba}_5\text{Ru}_2\text{O}_{11}$  showing alternance of  $\text{BaO}_3$  layers and  $\text{Ba}_2\text{O}_2$  layers. **b.** Peroxide groups in  $\text{Ba}_2\text{O}_2$  layers statistically distributed over three possible configurations (shown in gray), one of them being shown in red. **c.**  $\text{Ba}_2\text{O}$  layers replacing the  $\text{Ba}_2\text{O}_2$  layers to form  $\text{Ba}_5\text{Ru}_2\text{O}_{10}$ .

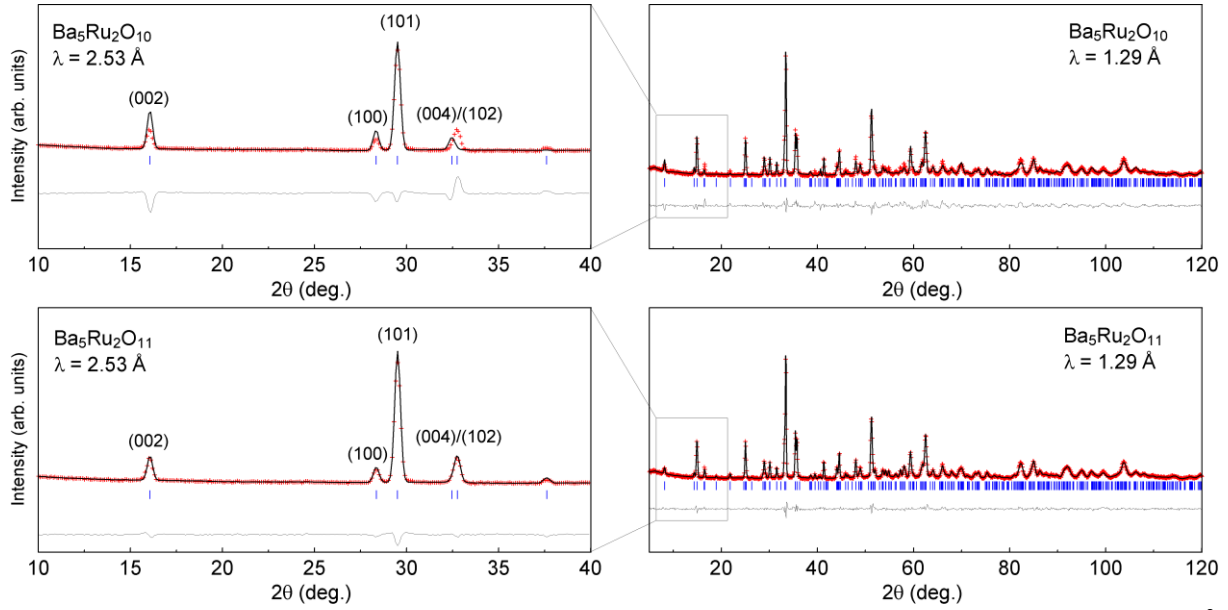


**Figure 3:** Rietveld refinement of the neutron diffraction patterns recorded with  $\lambda = 1.29 \text{ \AA}$  and  $\lambda = 2.53 \text{ \AA}$ . The top panel shows the refinement obtained from the  $\text{Ba}_5\text{Ru}_2\text{O}_{10}$  structural model while the bottom one is performed from the  $\text{Ba}_5\text{Ru}_2\text{O}_{11}$  model. The red crosses, black continuous line and bottom green line represent the observed, calculated, and difference patterns, respectively. Vertical blue tick bars mark the reflection positions.

**Table 1.** Structural parameters for  $\text{Ba}_5\text{Ru}_2\text{O}_{11}$ , deduced from the combined Rietveld refinement of the neutron diffraction patterns recorded with  $\lambda = 1.29 \text{ \AA}$  and  $\lambda = 2.53 \text{ \AA}$  at 300K.

---

$\text{Ba}_5\text{Ru}_2\text{O}_{11}$ ; Space Group:  $P 6_3/m m c$

$a = 5.9562(2) \text{ \AA}$ ,  $c = 18.0779(8) \text{ \AA}$ ,  $V = 555.41(4) \text{ \AA}^3$

---

Atom	Wyckoff site	$x$	$y$	$z$	$B(\text{\AA}^2)$	Occ
Ba1	4e	0	0	0.1389(4)	0.22(13)	1
Ba2	2c	1/3	2/3	1/4	0.05(18)	1
Ba3	4f	1/3	2/3	0.0158(4)	1.14(16)	1
Ru1	4f	1/3	2/3	0.6738(2)	0.28(9)	1
O1	6h	0.1842(9)	0.3684(9)	3/4	0.80(10)	1
O2	12k	0.4901(6)	0.9802(6)	0.61806(19)	0.83(6)	1
O3	12k	0.0782(10)	0.1565(10)	-0.0024(9)	0.9(3)	1/3

---

dataset  $\lambda = 1.29 \text{ \AA}$ : Bragg R-factor= 6.19%, Rf-factor= 4.65%;

dataset  $\lambda = 2.53 \text{ \AA}$ : Bragg R-factor= 3.57%, Rf-factor= 3.52%

---

Scanning transmission electron microscopy (STEM) was employed to analyze the local oxygen coordination environment in the structure. Complementary high angle annular dark-field and annular bright field STEM (HAADF-STEM and ABF-STEM) images of the material along the  $[10\bar{1}0]$  direction are shown in Figs. 4a,b. The HAADF-STEM images highlight projected positions of the heavy atomic columns, i.e. Ru and Ba, while the ABF-STEM images also contain signal from the light O columns. The HAADF-STEM image confirms the cationic arrangement of the material, corresponding to the layered 2H hexagonal perovskite type structure. In the image, BaO and Ru columns inside the perovskite blocks form a characteristic chevron pattern on three BaO (slightly brighter) and two Ru columns. The perovskite blocks are separated by planar interfaces of double Ba column, corresponding to the  $\text{Ba}_2\text{O}_2$  layers. In the ABF-STEM image, O columns inside the perovskite blocks produce sharp and well-defined spots next to the Ru columns, while the O signal in the  $\text{Ba}_2\text{O}_2$  layers is less pronounced. According to the theoretical ABF-STEM images (Figs. 4d,f), the difference between the  $\text{Ba}_5\text{Ru}_2\text{O}_{11}$  and  $\text{Ba}_5\text{Ru}_2\text{O}_{10}$  models is very subtle and pertains to the intensity of the O signal in the  $\text{Ba}_2\text{O}_2$  layers. While the simulations for both models reproduce well the overall appearance of the experimental images, neither of them is a direct match. A close comparison of the experimental and the theoretical HAADF-STEM and ABF-STEM images reveal two major differences: 1) in the experimental images, the projected Ba columns in the  $\text{Ba}_2\text{O}_2$  layers are somewhat smeared in the (001) plane compared to those in the perovskite blocks and 2) the intensity of the O columns in the experimental ABF-STEM is not exactly centered in-between the Ba columns. Taking into account that the signal from light atomic columns in ABF-STEM images is very sensitive to the long range ordering of the structure,<sup>39</sup> these discrepancies indicate that the peroxide species in the  $\text{Ba}_2\text{O}_2$  layered are either statistically distributed or dynamic. Either way, these static/dynamic O displacements

apparently affects the adjacent Ba positions as well, which is consistent with the crystal structure analysis using NPD data, showing elevated thermal displacement parameter for the corresponding Ba3 positions (Table 1).

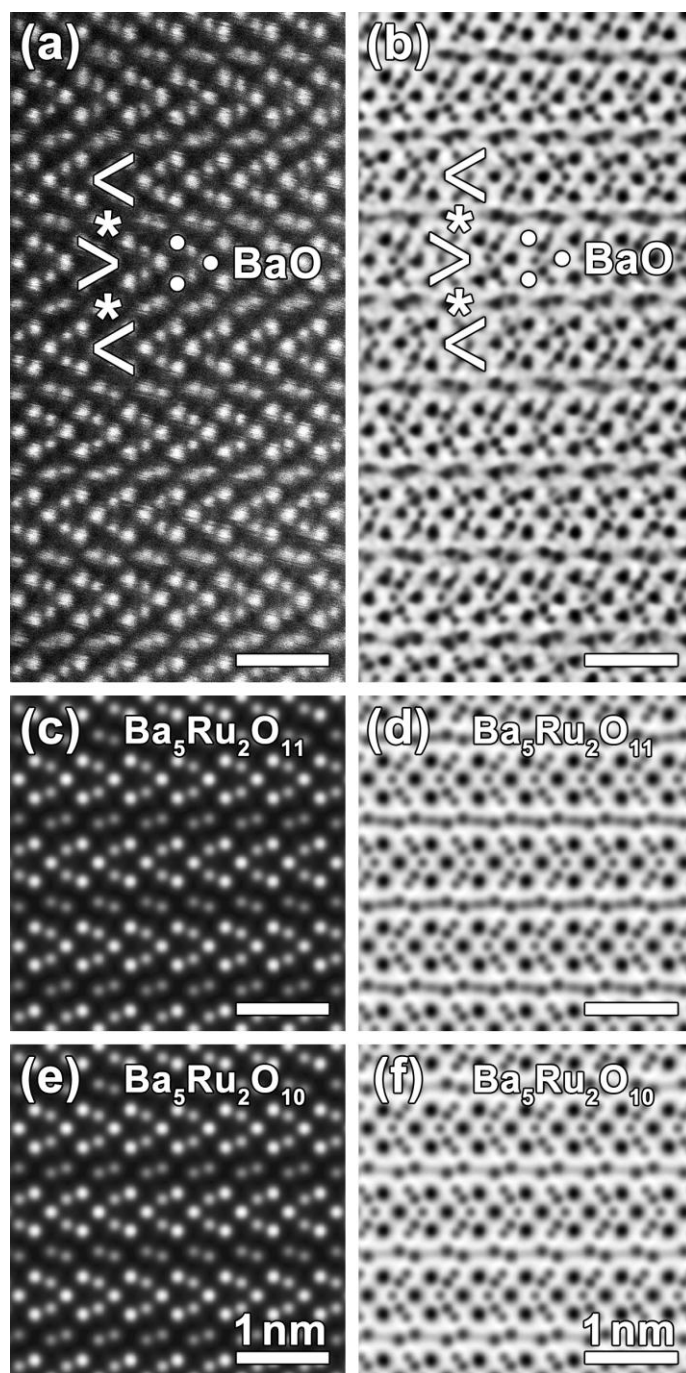


**Figure 4:** Experimental [10 $\bar{1}0$ ] HAADF-STEM (a) and ABF-STEM (b) images of the pristine Ba<sub>5</sub>Ru<sub>2</sub>O<sub>11</sub> compound investigated in this work, together with theoretical images calculated using structure model for the Ba<sub>5</sub>Ru<sub>2</sub>O<sub>11</sub> (c,d) and Ba<sub>5</sub>Ru<sub>2</sub>O<sub>10</sub> (e,f) compounds. In the experimental images, perovskite blocks are highlighted with chevrons made up of 3 BaO (marked with circles) and 2 Ru columns; the Ba<sub>2</sub>O<sub>2</sub> layers between the perovskite blocks are marked with asterisks. Note the presence of additional dots in ABF-STEM images (compared to HAADF-STEM) next to the Ru columns, corresponding to the O columns. Together with the O atoms in the BaO these O positions form projection of the RuO<sub>6</sub> octahedra.

Following this structural study, we analyzed the electronic signature of the peroxo-groups by means of X-ray absorption spectroscopy (XAS), Raman spectroscopy and density functional theory (DFT) calculations. X-ray absorption near edge structure (XANES) measurements at the Ru K-edge (Fig. 5a) confirmed ruthenium to be in an oxidation state of 5+ by comparing the edge position with Li<sub>2</sub>Ru<sup>4+</sup>O<sub>3</sub>, Li<sub>3</sub>Ru<sup>5+</sup>O<sub>4</sub>, La<sub>2</sub>LiRu<sup>5+</sup>O<sub>6</sub> and Na<sub>2</sub>Ru<sup>6+</sup>O<sub>4</sub> reference compounds. Furthermore, the appearance of a small pre-edge peak at about 22120 eV, as already observed for Li<sub>3</sub>RuO<sub>4</sub>,<sup>40</sup> reveals the non-centrosymmetric position of ruthenium atom in the RuO<sub>6</sub> octahedra (Fig. 5b) due to the short distances between the centers of the octahedra sharing faces. This is confirmed by the analysis of the extended X-ray absorption fine structure (EXAFS) oscillations (Fig. 5b). Then, using Raman spectroscopy, a vibration at about 800 cm<sup>-1</sup> characteristic of O-O bond stretching<sup>41</sup> was found for the pristine compound (Fig. S1). Finally, DFT calculations were carried out using the structure of Ba<sub>5</sub>Ru<sub>2</sub>O<sub>11</sub> refined by NPD (Fig. 6). The atom-projected density of states (pDOS) shows RuO\* states above the Fermi level with a predominant Ru character (Fig. 6a). This is confirmed by the positive Fukui function, a probe of the lowest unoccupied states (see methods), which reveals that the states involved in the reduction (electron addition) are t<sub>2g</sub>-like local levels (Fig. 6b). Below the Fermi level, pDOS evidences a larger oxygen character with O(*p*) states being even greater than Ru(*d*) states around -1.5 eV,

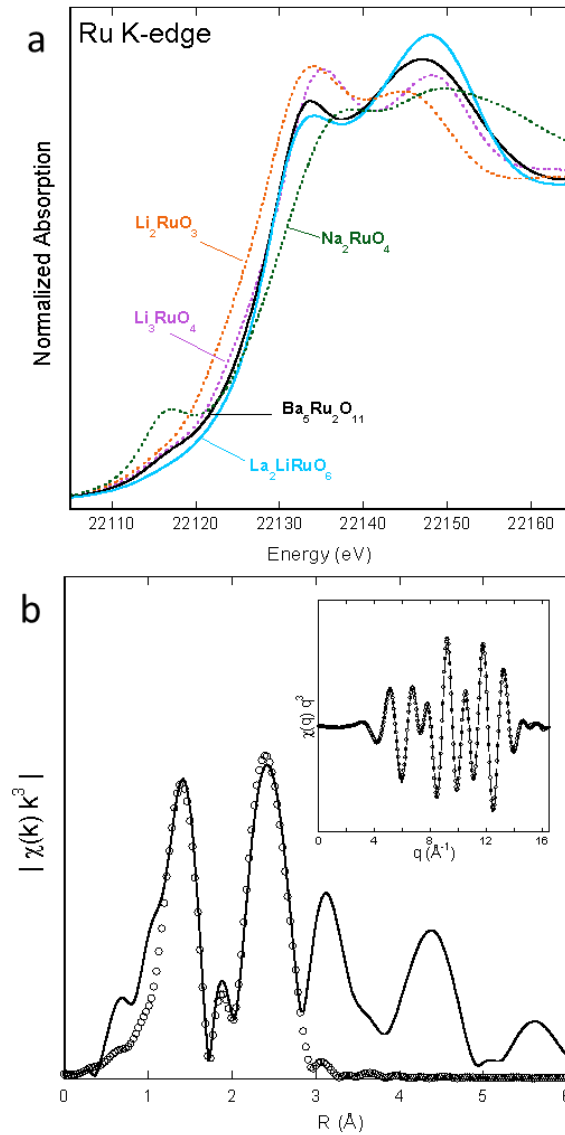


**Figure 5:** a Ru K-edge XANES spectra of  $\text{Ba}_5\text{Ru}_2\text{O}_{11}$  compared to  $\text{Ru}^{5+}$ -containing perovskite  $\text{La}_2\text{LiRuO}_6$ ,  $\text{Ru}^{5+}$ -containing rock salt  $\text{Li}_3\text{RuO}_4$ ,  $\text{Ru}^{4+}$ -containing layered compound  $\text{Li}_2\text{RuO}_3$  and  $\text{Na}_2\text{Ru}^{6+}\text{O}_4$  b Magnitude of Fourier transform (FT) of  $k^3$ -weighted EXAFS oscillations (solid line) of  $\text{Ba}_5\text{Ru}_2\text{O}_{11}$  along with fitting results (open circles). In inset shows the filtered EXAFS oscillations in the  $q$  space. The FT is not corrected for phase shifts.

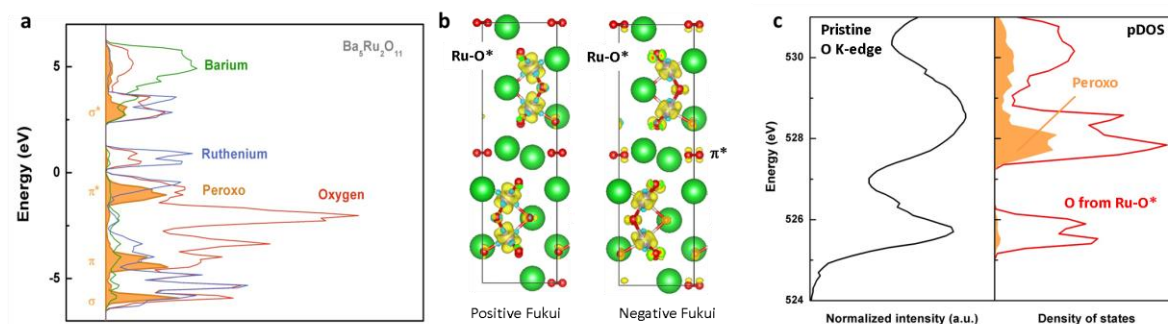


**Figure 6:** **a.** Atom-projected density of states (pDOS) computed from DFT for Ba<sub>5</sub>Ru<sub>2</sub>O<sub>11</sub> where the oxide ions and ruthenium cations from the RuO<sub>6</sub> octahedra (red and blue, respectively) are differentiated from peroxide (O<sub>2</sub>)<sup>2-</sup> groups in the Ba<sub>2</sub>O<sub>2</sub> planes (plain orange). **b.** Negative and positive Fukui functions rendering the electronic density upon electron removal or addition, respectively, where Ru-O\* orbitals are polarized upon reduction (positive Fukui) and Ru-O\* as well as O-O π\* states are polarized upon oxidation (negative Fukui). **c.** X-ray absorption spectrum at the O K-edge in the fluorescence mode for the pristine Ba<sub>5</sub>Ru<sub>2</sub>O<sub>11</sub> compared with the pDOS for oxygen and peroxo-groups.

indicating that in addition to the RuO\* states, non-bonding oxygen states may lie below the Fermi level as previously discussed for other Ru-based compounds and observed in the Elf function (Fig. S2).<sup>9,42</sup> Furthermore, pDOS also reveals four narrow bands associated with the peroxo-groups, namely the σ\*, π\*, π and σ from high to low energy, with the σ\* and π\* states lying respectively above and below the Fermi level (Fig. 6a). The negative Fukui function confirms the involvement of t<sub>2g</sub>-like RuO\* local level in oxidation (electron removal), but also shows the π\* oxygen states from the peroxide groups to be polarized upon electron removal (Fig. 6b). From this computational study, several conclusions can already be drawn. First, O<sub>2</sub><sup>2-</sup> peroxo-groups can potentially be oxidized which would eventually lead to the condensation of O<sub>2(g)</sub>. Second, these peroxo-groups can hardly be reduced into O<sup>2-</sup> due to the destabilization of the σ\* empty states above the Ru-O antibonding t<sub>2g</sub> states. This effect is critical since it will likely limit the reversibility of electrochemical reactions when the O<sub>2</sub><sup>2-</sup>/O<sup>2-</sup> redox couple is used as redox center for Li-ion battery materials or as OER redox active

sites. Indeed, when the TM-O antibonding states lie between the  $\pi^*$ - $\sigma^*$  gap for peroxo-groups, the electrochemical reduction would first affect the TM-O antibonding states prior to the  $\sigma^*$  states from the peroxo-groups, following a linear response theory. Owing to the generally large  $\pi^*$ - $\sigma^*$  gap for peroxo-groups (above 2 eV for  $\text{Li}_2\text{O}_2$  for instance<sup>43</sup>), obtaining an active  $\text{O}_2^{2-}/\text{O}^{2-}$  redox couple in TM-based material is unfortunately unlikely. However, as the  $\pi^*$ - $\sigma^*$  gap decreases with the increase of the O-O distance,  $\text{O}_2^{n-}/\text{O}^{2-}$  redox couple (with  $n > 2$ ) can be activated as long as the  $\sigma^*$  state lay below the TM-O antibonding states. To further support the computed DOS, XAS at the O K-edge was performed and compared with the DOS above the Fermi level (Fig. 6c). At around 526 eV, the first absorption peak can be assigned to the dipole transition from O(1s) states to the  $t_{2g}$ -like  $\text{RuO}^*$  states with a predominant Ru character. At higher energy  $\approx 529$  eV, a second and broader absorption peak can be observed. When compared to the computed DOS, this peak could be attributed to the overlap of two absorption peaks corresponding to the transitions O(1s) to  $\text{RuO}^*$  states and O(1s) to  $\text{O}_2^{2-} \sigma^*$  states. These spectra will be discussed later on in more detail.

To shine the light on the complex redox properties of these peroxo-groups, electrochemical measurements were then carried out. First,  $\text{Ba}_5\text{Ru}_2\text{O}_{11}$  was used as an oxygen electrocatalyst in different aqueous media (Fig. 7). Under OER conditions at pH 13 (0.1 M KOH), a very limited electrocatalytic activity could be detected (dark blue in Fig. 7b). While this observation is consistent with our previous observation that  $\text{Ru}^{5+}$ -containing perovskites  $\text{La}_2\text{LiRuO}_6$  was not active in alkaline conditions,<sup>6</sup> it also indicates that the peroxo-groups are not active as redox center under these conditions. Ex situ atomic resolution HAADF-STEM imaging indicate that, aside from a slight amorphous surface, which is typical for hexagonal perovskites,<sup>44</sup> cycling under OER conditions at pH 13 does not induce drastic modifications in

the bulk structure (Fig. S3). We thus decided to cycle the compound under reductive conditions at pH 13 (red curve in Fig. 7a). Two successive reduction waves can be observed. The first reduction at about 0.3 V vs. NHE (about 3.3 V vs. Li<sup>+</sup>/Li) is associated with an oxidation peak (light blue curve in Fig. 7c), presumably corresponding to the Ru<sup>5+</sup>/Ru<sup>4+</sup> redox couple balanced by the formation of oxygen defects. Interestingly, triggering this redox induces a large increase in the oxidation current above E°(O<sub>2</sub>/HO<sup>-</sup>) (0.463 V vs. NHE at pH 13). Nevertheless, when pushing the electrochemical window to higher potential by decreasing the pH to 7 (green curve in Fig. 7d), two oxidation waves can be observed. Even though two corresponding reduction waves are observed in the backward scan, the drastic

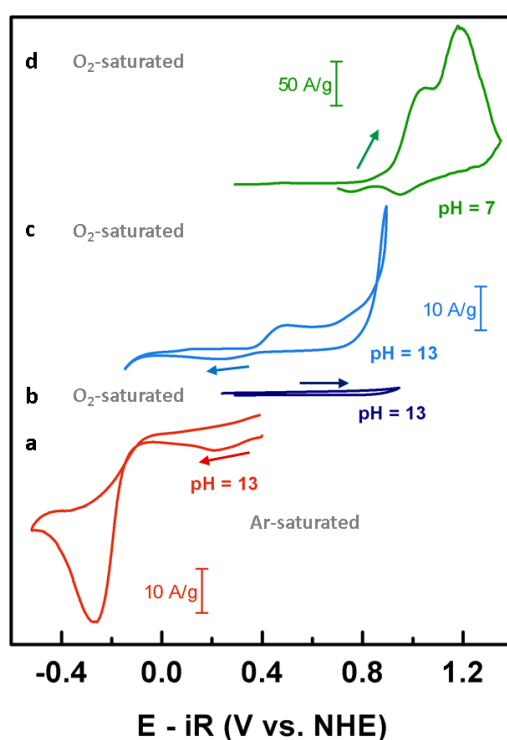


**Figure 7:** Aqueous electrochemistry of Ba<sub>5</sub>Ru<sub>2</sub>O<sub>11</sub> at different pH and under positive or negative polarization. **a** under Ar-saturated solution at pH 13, starting under cathodic polarization, **b** under O<sub>2</sub>-saturated solution at pH 13 starting in anodic polarization, **c** under O<sub>2</sub>-saturated solution at pH 13 starting in cathodic polarization and **d** in O<sub>2</sub>-saturated solution at pH 7 starting in anodic polarization. E°(H<sub>2</sub>O/O<sub>2</sub>) at pH 13 is equal to 0.463 V vs. NHE and at pH 7 equal to 0.817 V vs. NHE. Arrows are guide for the initial polarization of each curve.

drop in current measured during the subsequent cycles (Fig. S4) as well as ex situ XRD measurement demonstrate the instability of the phase under such oxidizing conditions (Fig. S5). The decomposition is further confirmed by TEM data, which show that only a small portion of  $\text{Ba}_5\text{Ru}_2\text{O}_{11}$  could be found in the sample after cycling at pH 7 (Fig. S3). All together, these observations rule out oxygen evolution from the oxidation of water as the sole origin for the oxidative current observed at pH 13. From the negative Fukui function discussed above, this oxidation process could be related to both the  $\text{Ru}^{6+}/\text{Ru}^{5+}$  and  $\text{O}_{2(\text{g})}/\text{O}_2^{2-}$  redox couples. These processes being irreversible, they are certainly detrimental for the stability of the phase. Going back to the reduction at pH 13, a second reduction wave can be observed at -0.2 V vs. NHE in Ar-saturated solution (red curve in Fig. 7a). Similarly to the oxidation phenomenon, accessing the second reduction potential triggers instability of the phase, as seen in subsequent cycles.

To further unravel the complexity of these redox processes,  $\text{Ba}_5\text{Ru}_2\text{O}_{11}$  was then cycled in aprotic electrolyte (1M  $\text{LiPF}_6$  EC:DMC) where the behavior in oxidation was studied first (Fig. 8a). When oxidizing  $\text{Ba}_5\text{Ru}_2\text{O}_{11}$  with no initial reaction with  $\text{Li}^+$ , a plateau at about 3.3 V vs.  $\text{Li}^+/\text{Li}$  is observed. When monitoring the gas pressure during this plateau (Fig. S6), an increase in pressure could be observed, presumably owing to oxygen release given that the oxidation voltage is within the electrolyte stability window. A similar plateau could be observed in oxidation with a relaxed potential of about 2.6 V vs.  $\text{Li}^+/\text{Li}$ , after reduction for a capacity corresponding to the reaction with 2  $\text{Li}^+$  (Fig. 8a). Therefore, this plateau is associated with the direct oxidation of  $\text{Ba}_5\text{Ru}_2\text{O}_{11}$ . The charge balance upon oxidation could presumably be achieved through the removal of  $\text{Ba}^{2+}$  cations together with the direct oxidation of lattice peroxide groups leading to the loss of  $\text{O}_{2(\text{g})}$ . The aforementioned reaction

could then be compared with the simple reaction  $Ba^{2+} + O_{2(g)} + 2e^{-} = BaO_2$  ( $\Delta G_{formation} = -578$  kJ/mol at 298K) which would give a standard potential of about 3.12 V vs.  $Li^+/Li$ . This charge balance mechanism would be consistent with TEM data which demonstrate drastic instability triggered by this oxidation process (Fig. 9b), where the integrity of particles was found to be affected while leaving the crystal structure of the unaffected areas intact.

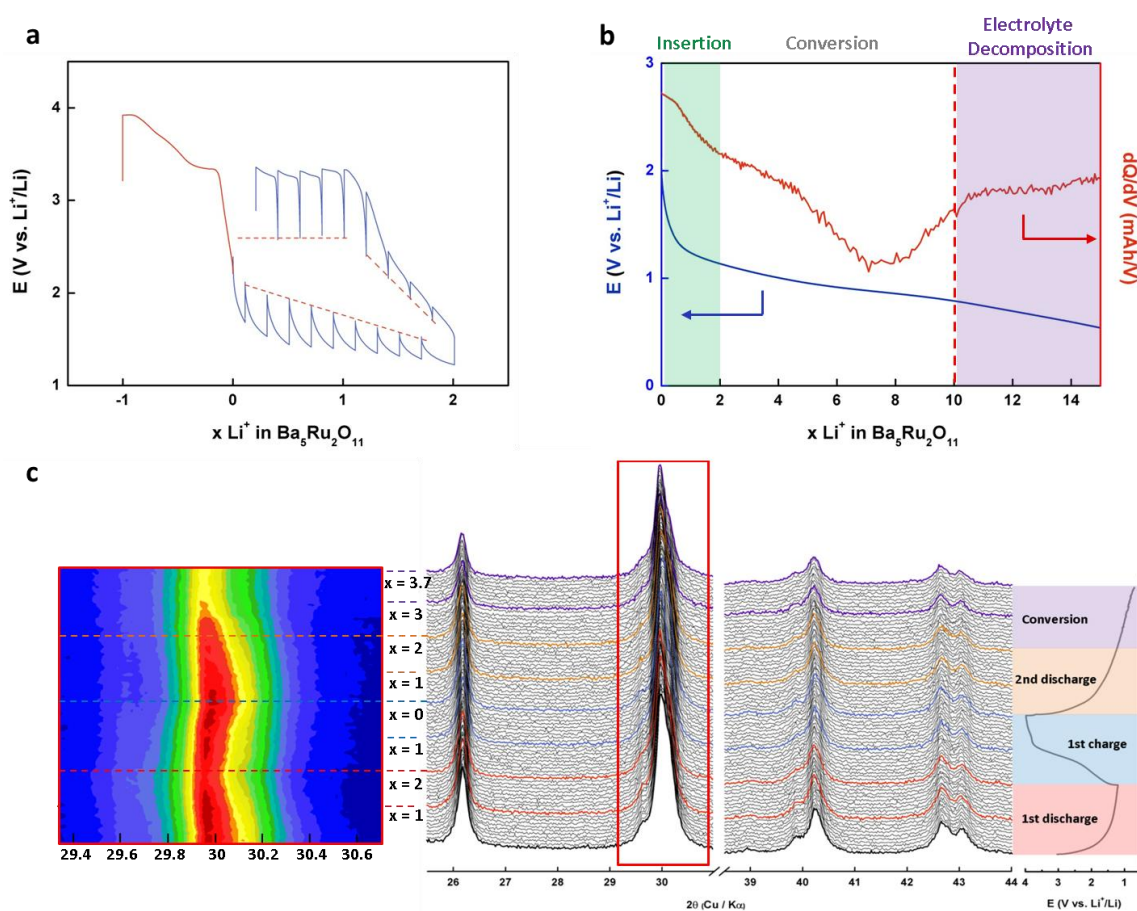


**Figure 8:** Electrochemistry of  $Ba_5Ru_2O_{11}$  in organic electrolytes EC:DMC (1:1) 1M  $LiPF_6$ , with **a** a charge at  $C/10$  (red) with no initial discharge, compared to a GITT curve of the processes initiated by reduction of the pristine phase, with pulses corresponding to  $C/10$  over  $0.2 Li^+$  followed by a 6 hours relaxation time in discharge then charge (blue). **b** a full discharge over  $10 Li^+$  equivalents corresponding to the full conversion into metallic ruthenium and its corresponding derivative curve  $dQ/dV$  **c** In situ XRD for  $Ba_5Ru_2O_{11}$  in EC:DMC (1:1) 1M  $LiPF_6$ , with a first cycle starting in discharge, limited to  $2 Li^+$  equivalents, followed by a second discharge over  $4 Li^+$  equivalents. A contour plot for the most intense peak at around  $30^\circ$  is provided on the left.

Turning back to the reactivity of  $\text{Ba}_5\text{Ru}_2\text{O}_{11}$  with  $\text{Li}^+$  in reduction, the galvanostatic discharge profile with a current density corresponding to C/5 (1 Li exchanged in 5 hours) shows a sloping discharge from the OCV to the cut-off voltage (Fig. 8b). From the derivative curve  $dQ/dV$ , it could be inferred that several processes take place during the reduction. Before the large reduction peak observed for  $2 \leq \text{Li} \leq 10$  corresponding to the complete conversion of  $\text{Ba}_5\text{Ru}_2\text{O}_{11}$  into metallic Ru, a sloping behavior is observed. In situ XRD measurements were then carried out in the range  $0 \leq \text{Li} \leq 2$  (Fig. 8c), suggesting that no drastic structural reorganization is encountered during the cycling of  $\text{Ba}_5\text{Ru}_2\text{O}_{11}$  in this range, both in charge and in discharge. However, peak intensity was found to reversibly decrease while peaks position shifts. This behavior is in contrast with the drastic decrease in the peak intensity observed for  $x > 2$  in discharge, which corresponds to the decomposition of the phase upon conversion. Hence, the electrochemical signature observed for  $0 \leq \text{Li} \leq 2$  could originate from the reversible insertion of Li, as previously observed for bulk  $\text{RuO}_2$ .<sup>45</sup> Nevertheless, we could see that this reactivity (presumably insertion) with  $\text{Li}^+$  leads to poor cyclability where only 1 Li could be extracted back (Fig. 8a) and the cycling performances were found to quickly decrease (Fig. S7). In the meanwhile, high-resolution HAADF-STEM images (Fig. 9) show that the reactivity of  $\text{Ba}_5\text{Ru}_2\text{O}_{11}$  with 2 Li preserves its atomic arrangement, but results in pronounced corrugation of the layers. Apparently, this transformation is associated with the deformation of the  $\text{Ba}_2\text{O}_2$  layers over few tens of nm, which indicate insertion of  $\text{Li}^+$  and reduction of the  $\text{Ba}_2\text{O}_2$  layers during the reactivity with Li. Nevertheless, part of the bulk remains unreacted (Fig. 9a), certainly owing to the poor  $\text{Li}^+$  diffusivity into this hexagonal perovskite.

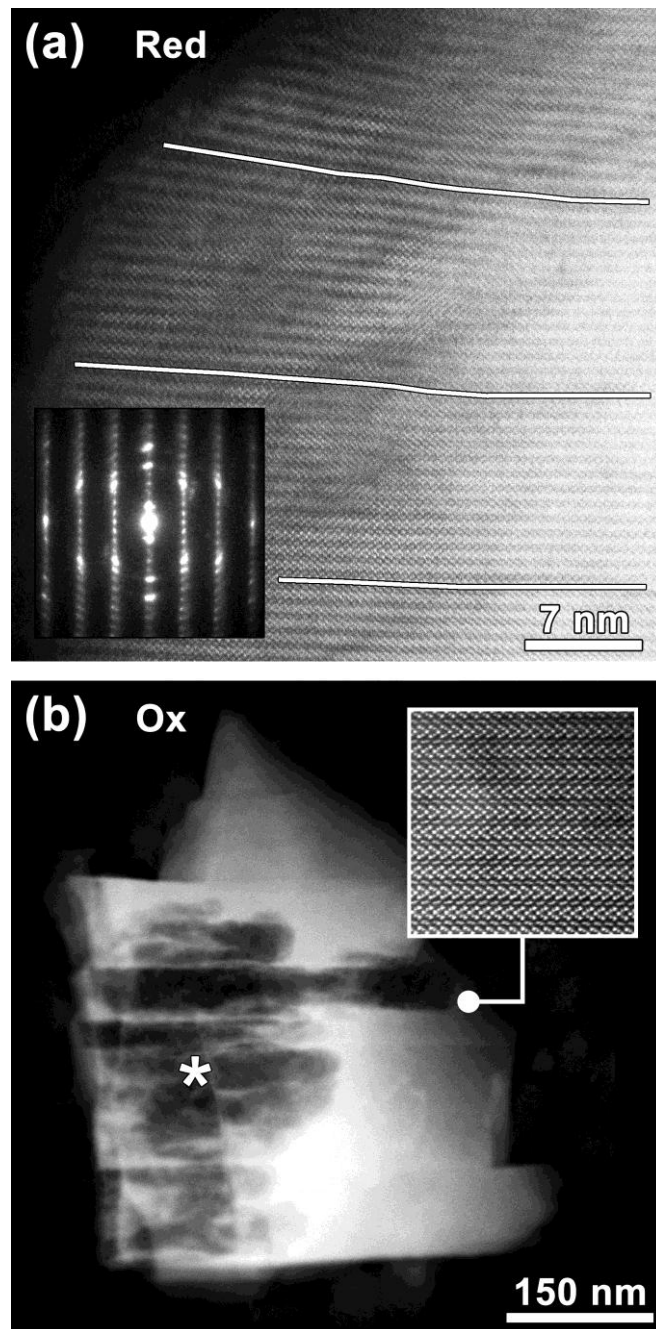


**Figure 9:** HAADF-STEM images taken along the  $[10\bar{1}0]$  zone axis of  $\text{Ba}_5\text{Ru}_2\text{O}_{11}$  after electrochemical reduction (a) and oxidation (b) in non-aqueous medium. In image (a), lines highlight corrugation of the perovskite blocks due to swelling of the  $\text{Ba}_2\text{O}_2$  layers; and the inset shows the corresponding ED pattern with characteristic tangential smearing of the Bragg reflections. Image (b) is representative low magnification image. It demonstrates that a large portion of the particle is missing (marked with an asterisk); and the inset shows a high resolution HAADF-STEM image, confirming that the crystal structure of the material is preserved in the area unaffected by the dissolution.

The redox processes occurring upon reduction and oxidation for  $\text{Ba}_5\text{Ru}_2\text{O}_{11}$  were further assessed by means of ex situ XAS measurements at the Ru K-edge and O K-edge (Fig. 10). First, the Ru K-edge XANES spectra were found to remain unchanged after direct oxidation of  $\text{Ba}_5\text{Ru}_2\text{O}_{11}$  (Fig. 10a), consistent with our assumption that the oxidation is counterbalanced by oxygen release and compound dissolution, only leaving intact portions of the  $\text{Ru}^{5+}$ -containing pristine  $\text{Ba}_5\text{Ru}_2\text{O}_{11}$  phase. Upon reduction, no shift in the Ru K-edge was observed after the reactivity with 1 Li, while a slight shift of the edge towards lower energy was observed after the reactivity with 2 Li. This shift can be better seen when looking at the derivative of the normalized absorption (inset in Fig. 10a), and would indicate a reduction of  $\text{Ru}^{5+}$  upon reactivity with  $\text{Li}^+$ . Moreover, no significant modifications in the EXAFS oscillations were found, indicating minimal distortions of the local structure upon reduction (Fig. 10b). Overall, these observations highlight the reactivity of  $\text{Ba}_5\text{Ru}_2\text{O}_{11}$  with Li, which is nevertheless limited to the first few nanometers as seen by TEM (Fig. 9). To further assess if the  $\text{O}_2^{2-}/\text{O}^{2-}$  redox couple is involved in reduction for the  $\text{Ba}_5\text{Ru}_2\text{O}_{11}$  phase, XAS measurements at the O K-edge were performed using fluorescent yield (FY) mode, which probes several tens of nm into the bulk of the samples (Fig. 10c). Looking at the O K-edge spectra recorded for the reduced and oxidized samples, two main peaks at 526 and 529 eV are observed. Upon cycling, the overall absorption intensity varies with a drastic drop of intensity measured in reduction. In details, the relative intensities for the peaks at 526 and 529 eV ascribed to the transition  $\text{O}(1s)$  to  $\text{Ru-O}^*$  states and a combination of transition  $\text{O}(1s)$  to  $\text{Ru-O}^*$  and  $\text{O}(1s)$  to peroxide  $\sigma^*$  empty states, respectively, were found to vary concomitantly (Fig. 10d). This observation excludes the reduction of the peroxide groups which would only impact the peak at around 529 eV. Instead, it could be indicative of both the accumulation of products formed on the surface upon reduction, as seen in the surface

sensitive total electron yield (TEY) mode (Fig. S8), and electron injection into Ru-O\* states. The latter is in agreement with the positive Fukui function (Fig. 6b) where only the Ru-O\* states were found to be polarized upon electron injection into Ba<sub>5</sub>Ru<sub>2</sub>O<sub>11</sub>, as well as with the XAS measurements at the Ru K-edge where partial reduction of Ru<sup>5+</sup> was observed (Fig. 10a). Overall, this study tends to confirm that the  $\sigma^*$  O-O states formed for the peroxide groups are destabilized at too high energy and presumably do not participate to the reduction process.

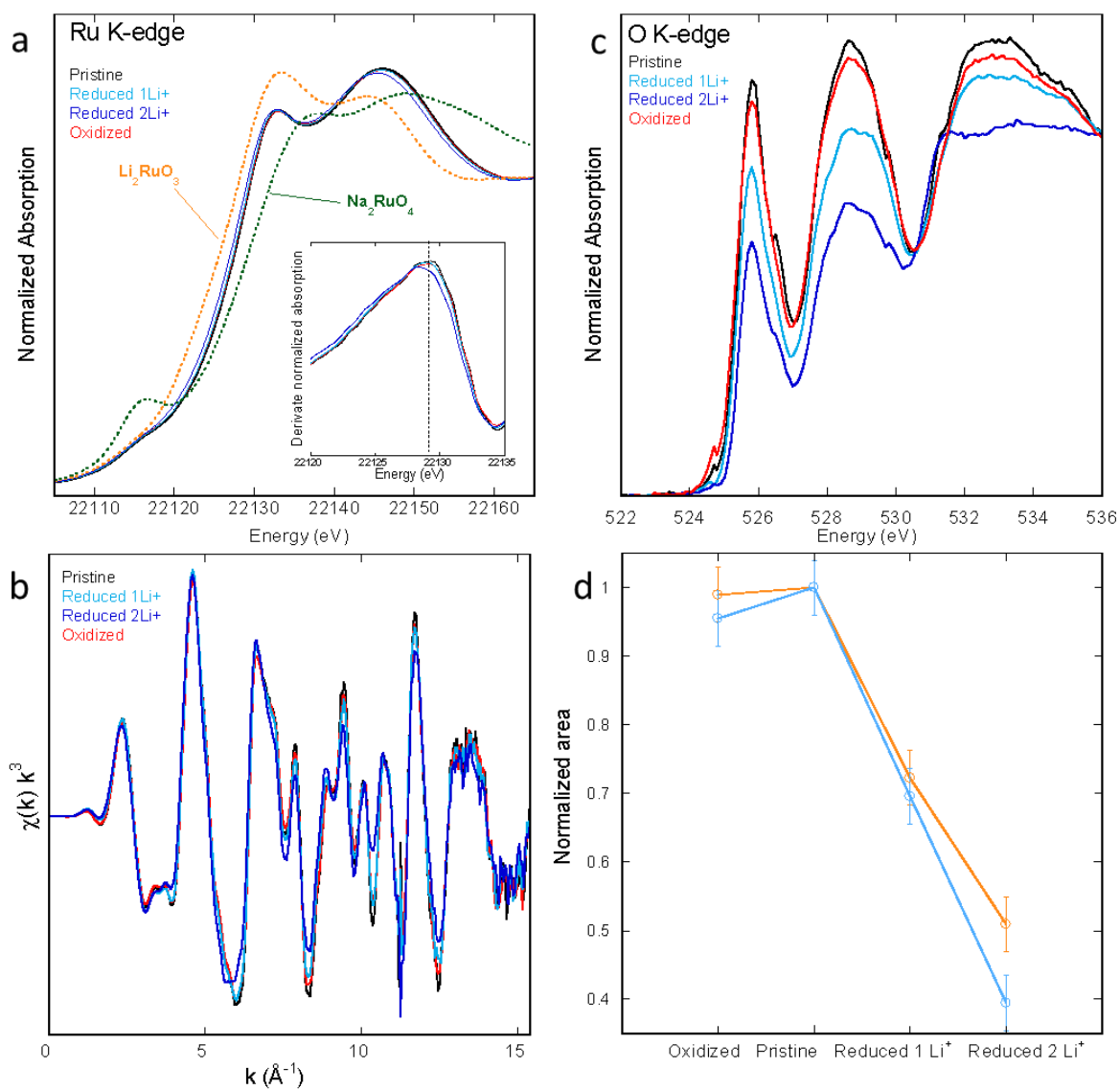


**Figure 10:** **a** Ru K-edge XANES spectra for pristine Ba<sub>5</sub>Ru<sub>2</sub>O<sub>11</sub> and the samples reduced with 1 Li<sup>+</sup>, 2 Li<sup>+</sup> or oxidized for the equivalent of 1 Ba<sup>2+</sup>. **b** Ru K-edge EXAFS oscillations weighted by k<sup>3</sup> of the pristine Ba<sub>5</sub>Ru<sub>2</sub>O<sub>11</sub> and ex situ samples. **c** O K-edge XAS spectra for pristine Ba<sub>5</sub>Ru<sub>2</sub>O<sub>11</sub> and ex situ samples. **d** Evolution upon cycling of the integrated areas for the absorption peak at about 526 eV (orange) and about 529 eV (blue) normalized compared to the peaks for the pristine compound.

In this study we demonstrate that the stabilization of peroxide (O<sub>2</sub>)<sup>2-</sup> groups in the pristine transition metal oxide is detrimental for the redox activity of materials used as water oxidation catalysts or Li-ion battery positive electrodes. When oxidizing lattice oxygen ions O<sup>2-</sup> to form peroxide (O<sub>2</sub>)<sup>2-</sup> groups during the charge of transition metal oxides used as positive electrode for Li-ion batteries, a concomitant destabilization of the σ\* empty O-O states at high energy would be expected to occur. These states lying well above the Fermi level become inactive upon reduction and are thus “frozen” inside the material, which then follows a cationic redox reaction in reduction. Furthermore, the π\* O-O states that are formed within the peroxide groups lie just below the Fermi level and introduce instabilities upon charge, where gaseous oxygen is presumably released. Owing to the bond order of 1 of the peroxide groups, the enthalpy required to release gaseous oxygen is therefore relatively positive and the potential for the redox couple O<sub>2</sub><sup>2-</sup>/O<sub>2</sub> relatively low, ranging from 2.5 to 3.2 V vs Li<sup>+</sup>/Li depending on the electrostatic interaction with the surrounding alkaline or alkaline-earth cations. Despite the relative ease to release gaseous oxygen, which could be seen as a blessing for the oxygen evolution reaction, the cationic loss required to keep the charge balance is detrimental for the stability of the structure and one can already foresee catalysts proceeding through a direct lattice oxygen oxidation as prone to surface instability and drastic dissolution.<sup>6,7,48,49</sup> Therefore, two scenarios appear as preferential for Li-ion battery materials and OER catalysts. For Li-ion battery positive electrodes, the reversible

formation of peroxo-like  $(\text{O}_2)^{n-}$  groups with a bond order lower than 1 and empty  $\sigma^*$  states lying just above the Fermi level appears as favorable when compared to the formation of actual peroxide groups. Unfortunately, despite the strong appeal for such anionic redox behavior, which enables higher storage of charge, slow kinetics in reduction<sup>50</sup> and surface instabilities for these groups are already foreseen.<sup>24,26</sup> For OER catalysts, the oxidation of lattice oxygen and the formation of oxyl  $\text{O}^{\bullet}$  radicals which would allow for a fast gaseous oxygen formation following an acid-base mechanism seems rather preferential, i.e. with the oxyl groups acting as electrophilic species while water acts as nucleophilic species. Indeed, it would be less destabilizing for the structure than a direct-coupling mechanism for which two oxidized lattice oxygen atoms form bond and eventually condensate to degas  $\text{O}_{2(\text{g})}$ <sup>22</sup> which would imply the partial decoordination of transition metals as triggered by the increasing bond order between lattice oxygen ions. We could therefore demonstrate that peroxo-containing  $\text{Ba}_5\text{Ru}_2\text{O}_{11}$  compound is unstable under OER conditions. Further work would be necessary in order to better understand the kinetics of these two mechanisms.

## Conclusion

Using  $\text{Ba}_5\text{Ru}_2\text{O}_{11}$  as a model compound, we could gain deeper insights into the redox behavior of peroxide groups in transition metal oxides used as OER catalysts and electrodes for Li-ion batteries. Combining physical and electrochemical characterizations, we could demonstrate that the destabilization of the empty  $\sigma^*$  states of the peroxide group unfortunately freezes these states at high energy above the  $\text{RuO}^*$  antibonding states and thus the peroxide  $(\text{O}_2)^{2-}$  cannot be reduced back to oxide ions. Upon oxidation, the peroxide groups whose  $\pi^*$  states lie just below the Fermi level are redox active, leading to an unstable

situation. This limitation eventually hampers the use of the  $O_2/O_2^{2-}$  redox couple and is in line with previous reports on the instability of high-valence iridium- and ruthenium-based oxides used as OER catalysts.<sup>6,51–54</sup> As a conclusion, peroxide groups as redox centers appear undesirable for OER catalysts and Li-ion battery materials. This study calls for new chemical approaches to avoid the formation of such states when oxidizing transition metal oxides and to stabilize lower bonded peroxy-like  $(O_2)^{n-}$  species with  $n$  being 3 (or  $O_3^{5-}$  groups, as described elsewhere<sup>18,55</sup>) for reversible Li-ion battery materials or highly reactive  $O^{\bullet-}$  radicals with no lattice O-O bond formation for OER catalysts. This could be realized by a control of the  $\pi^*-\sigma^*$  gap which is directly correlated to the O-O bond length and to the charge of the peroxy-like species, as already proposed in Li-rich M(4d)-based materials with the so-called reductive coupling mechanism. No doubt that the importance of finding such compounds for the development of the next generation of energy storage devices will still generate a lot of efforts.

## Methods

**Materials synthesis and powder diffraction.**  $Ba_5Ru_2O_{11}$  was synthesized by hand grinding  $RuO_2$  and  $BaCO_3$  precursors followed by thermal treatment at  $950^\circ C$  for 48 hours under  $O_2$ . Laboratory X-ray diffraction (XRD) patterns were recorded with a Bruker D8 Advance diffractometer equipped with a copper source ( $\lambda_{Cu-K\alpha 1} = 1.54056 \text{ \AA}$ ,  $\lambda_{Cu-K\alpha 2} = 1.54439 \text{ \AA}$ ) and a LynxEye detector. Neutron powder diffraction (NPD) experiments were performed on the D1B powder diffractometer at the Institut Laue Langevin (Grenoble, France), with two wavelengths of  $1.29 \text{ \AA}$  and  $2.53 \text{ \AA}$  with the powder placed in a  $\varnothing=6\text{mm}$  cylindrical vanadium

can. The recorded patterns were refined using the Rietveld method as implemented in the FullProf program.<sup>56–58</sup>

**Electrochemical measurements.** Aqueous measurements were carried out by drop-casting an ink made by mixing tetrahydrofuran (THF; Sigma-Aldrich 99,9%) with Ba<sub>5</sub>Ru<sub>2</sub>O<sub>11</sub> powder and ethylene black carbon (Alfa Aesar 99,9%) in a 5:1 weight ratio as well as Nafion binder (5% weight, Ion Power). For the measurements in alkaline solution, the Nafion was neutralized with KOH, whereas at neutral pH the Nafion was used as received. Glassy carbon electrodes with a surface of 0.196 cm<sup>2</sup> were used as support, with a loading of active material of 50 µg per electrode. Rotating disk electrode measurements were performed in glass cells previously cleaned by acid treatment following by boiling in water for 2 hours. A PINE Instrument device was used at 1600rpm. A solution of 0.1M KOH was used for pH = 13, while for measurements in neutral pH a 0.1M H<sub>2</sub>SO<sub>4</sub> solution was made into which 1 M KNO<sub>3</sub> was added to keep a high ionic strength and the solution adjusted to pH 7 by adding KOH pellets. All the measurements were carried out in Ar-saturated solutions. To prepare XRD and TEM samples, a high loading of 1 mg per electrode was used onto glassy carbon electrode with approximately 1 cm<sup>2</sup> size. The powder was collected after washing with ethanol and sonication.

Electrochemical studies in organic solvent were carried out in Swagelock-type cells with a Li metal counter electrode and LP30 electrolyte (BASF) which were assembled in an argon-filled glovebox. The active material was ball milled with 10% carbon black (Super P, Timcal) using a SPEX ball mill for 20 minutes. To prepare XAS and TEM samples, powder was collected after cycling and washed with dimethyl carbonate and centrifuged before drying under vacuum.

### **Transmission electron microscopy.**

Samples for transmission electron microscopy (TEM) were prepared by grinding materials in a mortar and dispersing the powder onto holey carbon TEM grids. Samples after electrochemical testing in non-aqueous solution were stored and prepared for TEM in argon atmosphere; and a special Gatan Vacuum Transfer holder was used for analysis. High angle annular dark-field, annual bright field scanning TEM (HAADF-STEM and ABF-STEM, respectively) and ED patterns were acquired using a probe aberration corrected FEI Titan<sup>3</sup> 80-300 electron microscope operated at 300 kV.

### **X-ray absorption spectroscopy.**

XAS measurements at the Ru K-edge were performed in transmission mode at the ROCK beamline<sup>59</sup> of synchrotron SOLEIL (France). A Si (220) channel-cut quick-XAS monochromator with an energy resolution of 2 eV at 22 keV was used. The intensity of the monochromatic X-ray beam was measured with three consecutive ionization detectors. The samples were placed between the first and the second ionization chambers. For each measurement, successive spectra were collected at a rate of 2 Hz and averaged out over periods of 5 minutes. The energy calibration was established with simultaneous absorption measurements on RuO<sub>2</sub>, placed between the second and the third ionization chambers. The data was treated using the Demeter package for energy calibration and normalization, and EXAFS oscillations were fitted using Artemis software.<sup>60</sup> Fourier transforms of EXAFS oscillations were carried out in k-range from 4.2 Å<sup>-1</sup> to 15.2 Å<sup>-1</sup>. Fitting was performed in R-range from 1.0 to 2.9 Å using k<sup>3</sup> weight. EXAFS amplitudes and phase-shifts were calculated by FEFF7 starting from the calculated lattice parameters of the structures determined by combined Rietveld refinement of the neutron patterns. Except the radial distance (R) and

the Debye-Waller factor ( $\sigma^2$ ), all other parameters were kept constant ( $N_i$ ,  $E_0$ ,  $S_0^2$ ) in the conventional least squares modelling using the phase and amplitude factors calculated by the FEFF7. For ex situ XAS measurements, each cycled electrode was placed between two layers of Kapton tape, which was then sealed inside the argon glovebox within two layers of airtight transparent plastic pouches.

XAS spectra at O K-edge were collected on beamline 4-ID-C of the Advanced Photon Source (APS) at Argonne National Laboratory. The ex situ cathodes were transferred from an Ar-filled glovebox to the measurement chamber using a vacuum-compatible stage. Normalization of the XAS spectra as well as the fitting procedure were done using the Athena software.<sup>60</sup> The absorption step was reproduced using an error function. Gaussian curves were used to fit the peak positions of the normalized XAS spectra.

### **First-principles DFT calculations.**

Spin-polarized density functional theory (DFT) calculations were performed using the plane-wave density functional theory VASP (Vienna ab initio simulation package) code<sup>61,62</sup> within the generalized gradient approximation of Perdew–Burke–Ernzerhof (PBE) to describe electron exchange and correlation.<sup>63</sup> The rotationally invariant Dudarev method<sup>64</sup> (DFT+U) was used to correct the self-interaction error of conventional DFT for correlated d-electrons. Crystal structures of the  $\text{Ba}_5\text{Ru}_2\text{O}_{11}$  phase were shown to be correctly reproduced at  $U_{\text{eff}} = U - J = 2$  eV for Ir ( $J = 1$  eV). Conjugate gradient energy minimization procedure were used to relax all atom coordinates and lattice parameters until the forces acting on each atom were less than  $1.10^{-3}$  eV/Å. A plane-wave cutoff of 600 eV was used to describe the atomic basis set, with well-converged k-point sampling for each compound. Fukui functions were

calculated from charge density difference between phases where 0.4 % of the total number of electrons have been added or removed.

The Fukui functions  $f^+(r)$  and  $f^-(r)$  describes the change in the electron density of a system due to the variation of charge (i.e. electron addition or removal). They are probes of the lowest unoccupied ( $f^+$ ) or highest occupied ( $f^-$ ) states of a system, and represent the first step of a nucleophilic or electrophilic reaction, respectively.<sup>65</sup>

### Supporting Information

Additional Raman spectra, ELF function, TEM images, electrochemical data, x-ray diffraction, gas analysis, soft x-ray absorption spectroscopy.

### Acknowledgements

We thank S. Belin of the ROCK beamline (financed by the French National Research Agency (ANR) as a part of the “Investissements d’Avenir” program, reference: ANR-10- EQPX-45; proposal #20160095) of synchrotron SOLEIL for her assistance during XAS measurements. Authors would also like to thank V. Nassif for her assistance on the D1B beamline.

A.G, G.R. and J.-M.T acknowledge funding from the European Research Council (ERC) (FP/2014)/ERC Grant-Project 670116-ARPEMA.

### References

- (1) Cook, T. R.; Dogutan, D. K.; Reece, S. Y.; Surendranath, Y.; Teets, T. S.; Nocera, D. G. Solar energy supply and storage for the legacy and nonlegacy worlds. *Chem. Rev.* **2010**, *110*, 6474–6502.

- (2) Larcher, D.; Tarascon, J.-M. Towards greener and more sustainable batteries for electrical energy storage. *Nat. Chem.* **2015**, *7*, 19–29.
- (3) Lewis, N. S.; Nocera, D. G. Powering the planet: Chemical challenges in solar energy utilization. *Proc. Natl. Acad. Sci.* **2006**, *103*, 15729–15735.
- (4) Grimaud, A.; Hong, W. T.; Shao-Horn, Y.; Tarascon, J.-M. Anionic redox processes for electrochemical devices. *Nat. Mater.* **2016**, *15*, 121–126.
- (5) Sathiya, M.; Rouse, G.; Ramesha, K.; Laisa, C. P.; Vezin, H.; Sougrati, M. T.; Doublet, M.-L.; Foix, D.; Gonbeau, D.; Walker, W.; Prakash, a S.; Ben Hassine, M.; Dupont, L.; Tarascon, J.-M. Reversible anionic redox chemistry in high-capacity layered-oxide electrodes. *Nat. Mater.* **2013**, *12*, 827–835.
- (6) Grimaud, A.; Demortiere, A.; Saubanere, M.; Dachraoui, W.; Duchamp, M.; Doublet, M.; Tarascon, J. Activation of surface oxygen sites on an iridium-based model catalyst for the oxygen evolution reaction. *Nat. Energy* **2017**, *2*, 16189.
- (7) Grimaud, A.; Diaz-Morales, O.; Han, B.; Hong, W. T.; Lee, Y.-L.; Giordano, L.; Stoerzinger, K. a.; Koper, M. T. M.; Shao-Horn, Y. Activating lattice oxygen redox reactions in metal oxides to catalyse oxygen evolution. *Nat. Chem.* **2017**, *9*, 457–465.
- (8) Pearce, P. E.; Perez, A. J.; Rouse, G.; Saubanère, M.; Batuk, D.; Foix, D.; McCalla, E.; Abakumov, A. M.; Tendeloo, G. Van; Doublet, M.; Tarascon, J.-M. Evidence for anionic redox activity in a tridimensional-ordered Li-rich positive electrode -Li<sub>2</sub>IrO<sub>3</sub>. *Nat. Mater.* **2017**, *16*, 580–587.
- (9) Saubanère, M.; McCalla, E.; Tarascon, J.-M.; Doublet, M.-L. The intriguing question of anionic redox in high-energy density cathodes for Li-ion batteries. *Energy Environ. Sci.* **2016**, *9*, 984–991.
- (10) Xie, Y.; Saubanère, M.; Doublet, M.-L. Requirements for reversible extra-capacity in Li-rich layered oxides for Li-ion batteries. *Energy Environ. Sci.* **2017**, *10*, 266–274.
- (11) Seo, D.-H.; Lee, J.; Urban, A.; Malik, R.; Kang, S.; Ceder, G. The structural and chemical origin of the oxygen redox activity in layered and cation-disordered Li-excess cathode materials. *Nat. Chem.* **2016**, *8*, 692–697.
- (12) Yabuuchi, N.; Nakayama, M.; Takeuchi, M.; Komaba, S.; Hashimoto, Y.; Mukai, T.; Shiiba, H.; Sato, K.; Kobayashi, Y.; Nakao, A.; Yonemura, M.; Yamanaka, K.; Mitsuhara, K.; Ohta, T. Origin of stabilization and destabilization in solid-state redox reaction of oxide ions for lithium-ion batteries. *Nat. Commun.* **2016**, *7*, 13814.
- (13) Yabuuchi, N.; Takeuchi, M.; Nakayama, M.; Shiiba, H.; Ogawa, M.; Nakayama, K.; Ohta, T.; Endo, D.; Ozaki, T.; Inamasu, T.; Sato, K.; Komaba, S. High-capacity electrode materials for rechargeable lithium batteries: Li<sub>3</sub>NbO<sub>4</sub>-based system with cation-disordered rocksalt structure. *Proc. Natl. Acad. Sci. U. S. A.* **2015**, *112*, 7650-7655.

- (14) Lee, E.; Persson, K. A. Structural and Chemical Evolution of the Layered Li-Excess  $\text{Li}_x\text{MnO}_3$  as a Function of Li Content from First-Principles Calculations. *Adv. Energy Mater.* **2014**, *4*, 1400498.
- (15) Chen, H.; Islam, M. S. Lithium Extraction Mechanism in Li-Rich  $\text{Li}_2\text{MnO}_3$  Involving Oxygen Hole Formation and Dimerization. *Chem. Mater.* **2016**, *28*, 6656–6663.
- (16) Cox, N.; Pantazis, D. A.; Neese, F.; Lubitz, W. Biological Water Oxidation. *Acc. Chem. Res.* **2013**, *46*, 1588–1596.
- (17) Cox, N.; Retegan, M.; Neese, F.; Pantazis, D. A.; Boussac, A.; Lubitz, W. Electronic structure of the oxygen-evolving complex in photosystem II prior to O-O bond formation. *Science*. **2014**, *345*, 804–808.
- (18) McCalla, E.; Abakumov, A. A.; Saubanere, M.; Foix, D.; Berg, E. J.; Rouse, G.; Gonbeau, D.; Novák, P.; van Tendeloo, G.; Dominko, R.; Tarascon, J.-M. Visualization and impact of O-O peroxo-like dimers in high capacity layered oxides for Li-ion batteries. *Science*. **2015**, *350*, 1516–1521.
- (19) Siegbahn, P. E. M. Nucleophilic water attack is not a possible mechanism for O – O bond formation in photosystem II. *Proc. Natl. Acad. Sci.* **2017**, *114*, 4966–4968.
- (20) Krewald, V.; Retegan, M.; Cox, N.; Messinger, J.; Lubitz, W.; Debeer, S.; Pantazis, D. A. Metal oxidation states in biological water splitting. *Chem. Sci.* **2015**, *6*, 1676–1695.
- (21) Romain, S.; Bozoglian, F.; Sala, X.; Llobet, A. Oxygen - Oxygen Bond Formation by the Ru-Hbpp Water Oxidation Catalyst Occurs Solely via an Intramolecular Reaction Pathway. *J. Am. Chem. Soc.* **2009**, *131*, 2768–2769.
- (22) Mavros, M. G.; Tsuchimochi, T.; Kowalczyk, T.; Mcisaac, A.; Wang, L.; Voorhis, T. Van. What Can Density Functional Theory Tell Us about Artificial Catalytic. *Inorg. Chem.* **2014**, *53*, 6386–6397.
- (23) Betley, T. A.; Wu, Q.; Voorhis, T. Van; Nocera, D. G. Electronic design criteria for O-O bond formation via metal-oxo complexes. *Inorg. Chem.* **2008**, *47*, 1849–1861.
- (24) Yabuuchi, N.; Yoshii, K.; Myung, S.; Nakai, I.; Komaba, S. Detailed Studies of a High-Capacity Electrode Material for rechargeable batteries,  $\text{Li}_2\text{MnO}_3\text{-LiCo}_{1/3}\text{Ni}_{1/3}\text{Mn}_{1/3}\text{O}_2$ . *J. Am. Chem. Soc.* **2011**, *133*, 4404–4419.
- (25) McCalla, E.; Sougrati, M. T.; Rouse, G.; Berg, E. J.; Abakumov, A.; Recham, N.; Ramesha, K.; Sathiya, M.; Dominko, R.; Van Tendeloo, G.; Novák, P.; Tarascon, J.-M. Understanding the Roles of Anionic Redox and Oxygen Release during Electrochemical Cycling of Lithium-Rich Layered  $\text{Li}_4\text{FeSbO}_6$ . *J. Am. Chem. Soc.* **2015**, *137*, 4804–4814.
- (26) Luo, K.; Roberts, M. R.; Hao, R.; Guerrini, N.; Pickup, D. M.; Liu, Y.-S.; Edström, K.; Guo, J.; Chadwick, A. V.; Duda, L. C.; Bruce, P. G. Charge-compensation in 3d-transition-

- metal-oxide intercalation cathodes through the generation of localized electron holes on oxygen. *Nat. Chem.* **2016**, *8*, 684-691.
- (27) Koga, H.; Croguennec, L.; Ménétrier, M.; Mannesiez, P.; Weill, F.; Delmas, C. Different oxygen redox participation for bulk and surface : A possible global explanation for the cycling mechanism of  $\text{Li}_{1.20}\text{Mn}_{0.54}\text{Co}_{0.13}\text{Ni}_{0.13}\text{O}_2$ . *J. Power Sources* **2013**, *236*, 250–258.
- (28) Assat, G.; Iadecola, A.; Delacourt, C.; Dedryvère, R.; Tarascon, J.-M. Decoupling Cationic – Anionic Redox Processes in a Model Li-Rich Cathode via Operando X - ray Absorption Spectroscopy. *Chem. Mater.* **2017**, *29*, 9714–9724.
- (29) Bediako, D. K.; Costentin, C.; Jones, E. C.; Nocera, D. G.; Savéant, J.-M. Proton-electron transport and transfer in electrocatalytic films. Application to a cobalt-based  $\text{O}_2$ -evolution catalyst. *J. Am. Chem. Soc.* **2013**, *135*, 10492–10502.
- (30) Surendranath, Y.; Kanan, M. W.; Nocera, D. G. Mechanistic Studies of the Oxygen Evolution Reaction by a Cobalt-Phosphate Catalyst at Neutral pH. *J. Am. Chem. Soc.* **2010**, *132*, 16501–16509.
- (31) Fierro, S.; Nagel, T.; Baltruschat, H.; Comninellis, C. Investigation of the oxygen evolution reaction on Ti /  $\text{IrO}_2$  electrodes using isotope labelling and on-line mass spectrometry. *Electrochem. commun.* **2007**, *9*, 1969–1974.
- (32) Wohlfahrt-Mehrens, M.; Heitbaum, J. Oxygen evolution on Ru and  $\text{RuO}_2$  electrodes studied using isotope labelling and on-line mass spectrometry. *J. Electroanal. Chem.* **1987**, *237*, 251–260.
- (33) Mefford, J. T.; Rong, X.; Abakumov, A. M.; Hardin, W. G.; Dai, S.; Kolpak, A. M.; Johnston, K. P.; Stevenson, K. J. Water electrolysis on  $\text{La}_{(1-x)}\text{Sr}_{(x)}\text{CoO}_{(3-\delta)}$  perovskite electrocatalysts. *Nat. Commun.* **2016**, *7*, 11053.
- (34) Rong, X.; Parolin, J.; Kolpak, A. A Fundamental Relationship between Reaction Mechanism and Stability in Metal Oxide Catalysts for Oxygen Evolution. *M. ACS Catal.* **2016**, *6*, 1153–1158.
- (35) Götzfried, T.; Reller, A.; Ebbinghaus, S. G. Structural and Magnetic Properties of Hexagonal Perovskites  $\text{La}_{1.2}\text{Sr}_{2.7}\text{MO}_{7.33}$  (M = Ru, Ir) Containing Peroxide Ions. *Inorg. Chem.* **2005**, *44*, 6550–6557.
- (36) Ebbinghaus, S. G.; Erztoument, C.; Marozau, I.  $\text{Ln}_2\text{Sr}_2\text{PtO}_{7+\delta}$  (Ln=La, Pr, and Nd): Three new Pt-containing [AnBn–1O3n]-type hexagonal perovskites. *J. Solid State Chem.* **2007**, *180*, 3393–3400.
- (37) Grasset, F.; Dussarrat, C.; Darriet, J.; Schweitzer, A. A. Preparation, thermal stability and crystal structure of a new ruthenium(V) oxide containing peroxide ions :  $\text{Ba}_2\text{Ru}_5\text{O}_9(\text{O}_2)$ . Structural relationships to the hexagonal-type perovskite. *J. Mater. Chem.* **1997**, *7*, 1911–1915.

- (38) Grasset, F.; Zakhour, M.; Darriet, J. Synthesis, crystal structure and magnetic properties of  $\text{Ba}_5\text{Ru}_2\text{O}_9(\text{O}_2)$ ,  $\text{Ba}_5\text{Nb}_2\text{O}_9(\text{O}_2)$  and  $\text{Ba}_5\text{Ru}_2\text{O}_{10}$  related to the perovskite-type structure, and structural relationships with corresponding sulfides. *J. Alloys Compd.* **1999**, *287*, 25–31.
- (39) Findlay, S. D.; Shibata, N.; Sawada, H.; Okunishi, E.; Kondo, Y.; Ikuhara, Y. Ultramicroscopy Dynamics of annular bright field imaging in scanning transmission electron microscopy. *Ultramicroscopy* **2010**, *110*, 903–923.
- (40) Jacquet, Q.; Perez, A.; Batuk, D.; Tendeloo, G. Van; Rouse, G.; Tarascon, J.M The  $\text{Li}_3\text{Ru}_y\text{Nb}_{1-y}\text{O}_4$  ( $0 < y < 1$ ) System: Structural Diversity and Li Insertion and Extraction Capabilities. *Chem. Mater.* **2017**, *29*, 5331–5343.
- (41) Montemore, M. M.; Spronsen, M. A. Van; Madix, R. J.; Friend, C. M.  $\text{O}_2$  Activation by Metal Surfaces : Implications for Bonding and Reactivity on Heterogeneous Catalysts. *Chem. Rev.* **2017**. *118*, 2816-2862.
- (42) Sathiya, M.; Abakumov, A.M.; Foix, D.; Rouse, G.; Ramesha, K.; Saubanère, M.; Doublet, M.L.; Vezin, H.; Laisa, C.; Prakash, A.S.; P.; Gonbeau, D.; Van Tendeloo. G.; Tarascon, J.-M. Origin of voltage decay in high-capacity layered oxide electrodes. *Nat. Mater.* **2015**, *14*, 230–238.
- (43) Viswanathan, V.; Thygesen, K. S.; Hummelshøj, J. S.; Nørskov, J. K.; Girishkumar, G.; McCloskey, B. D.; Luntz, A. C. Electrical conductivity in  $\text{Li}_2\text{O}_2$  and its role in determining capacity limitations in non-aqueous Li- $\text{O}_2$  batteries. *J. Chem. Phys.* **2011**, *135*, 214704.
- (44) Grimaud, A.; Carlton, C. E.; Risch, M.; Hong, W. T.; May, K. J.; Shao-horn, Y. Oxygen Evolution Activity and Stability of  $\text{Ba}_6\text{Mn}_5\text{O}_{16}$ ,  $\text{Sr}_4\text{Mn}_2\text{CoO}_9$ , and  $\text{Sr}_6\text{Co}_5\text{O}_{15}$  : The Influence of Transition Metal Coordination. *J. Phys. Chem. C* **2013**, *117*, 25926–25932.
- (45) Delmer, B. O.; Balaya, P.; Kienle, L.; Maier, J. Enhanced Potential of Amorphous Electrode Materials: Case Study of  $\text{RuO}_2$ . *Adv. Mater.* **2008**, *20*, 501–505.
- (46) Patoux, S.; Vannier, R.-N.; Mairesse, G.; Nowogrocki, G.; Tarascon, J.M. Lithium- and Proton-Driven Redox Reactions in BIMEVOX-Type Phases. *Chem. Mater.* **2001**, *13*, 500–507.
- (47) Strauss, F.; Rouse, G.; Batuk, D.; Tang, M.; Salager, E.; Draz, G.; Dominko, R.; Tarascon, J.M. Electrochemical behavior of  $\text{Bi}_4\text{B}_2\text{O}_9$  towards lithium-reversible conversion reactions without nanosizing. *Phys. Chem. Chem. Phys.* **2018**, *20*, 2330–2338.
- (48) Yang, C.; Grimaud, A. Factors Controlling the Redox Activity of Oxygen in Perovskites : From Theory to Application for Catalytic Reactions. *Catalysts* **2017**, *7*, 149.
- (49) Grimaud, A.; May, K. J.; Carlton, C. E.; Lee, Y.-L.; Risch, M.; Hong, W. T.; Zhou, J.; Shao-Horn, Y. Double perovskites as a family of highly active catalysts for oxygen evolution in alkaline solution. *Nat. Commun.* **2013**, *4*, 2439.

- (50) Assat, G.; Delacourt, C.; Alves Dalla Corte, D.; Tarascon, J.-M. Practical Assessment of Anionic Redox in Li-Rich Layered Oxide Cathodes: A Mixed Blessing for High Energy Li-Ion Batteries. *J. Electrochem. Soc.* **2016**, *163*, A2965–A2976.
- (51) Chang, S. H.; Danilovic, N.; Chang, K.-C.; Subbaraman, R.; Paulikas, A. P.; Fong, D. D.; Highland, M. J.; Baldo, P. M.; Stamenkovic, V. R.; Freeland, J. W.; Eastman, J. A.; Markovic, N. M. Functional links between stability and reactivity of strontium ruthenate single crystals during oxygen evolution. *Nat. Commun.* **2014**, *5*, 4191.
- (52) Cherevko, S.; Geiger, S.; Kasian, O.; Kulyk, N.; Grote, J.-P.; Savan, A.; Shrestha, B. R.; Merzlikin, S.; Breitbach, B.; Ludwig, A.; Mayrhofer, K. J. J. Oxygen and hydrogen evolution reactions on Ru, RuO<sub>2</sub>, Ir, and IrO<sub>2</sub> thin film electrodes in acidic and alkaline electrolytes: A comparative study on activity and stability. *Catal. Today* **2016**, *262*, 170–180.
- (53) Cherevko, S.; Zeradjanin, A. R.; Topalov, A. a.; Kulyk, N.; Katsounaros, I.; Mayrhofer, K. J. J. Dissolution of Noble Metals during Oxygen Evolution in Acidic Media. *ChemCatChem* **2014**, *6*, 2219–2223.
- (54) Kasian, O.; Grote, J.; Geiger, S.; Cherevko, S.; Mayrhofer, K. J. J. The Common Intermediates of Oxygen Evolution and Dissolution Reactions during Water Electrolysis on Iridium. *Angew. Chem. Int. Ed. Engl.* **2018**, *57*, 2488–2491.
- (55) Demourgues, A.; Weill, A.; Darriet, B.; Wattiaux, A.; Grenier, J.-C.; Gravereau, P.; Pouchard, M. Additional Oxygen Ordering in "La<sub>2</sub>NiO<sub>4.25</sub>" (La<sub>8</sub>Ni<sub>4</sub>O<sub>17</sub>). II. structural Features. *J. Solid State Chem.* **1993**, *106*, 330–338.
- (56) Rietveld, H. M. A profile refinement method for nuclear and magnetic structures. *J. Appl. Crystallogr.* **1969**, *2*, 65–71.
- (57) Rodriguez-Carvajal, J. Recent advances in magnetic structure determination by neutron powder diffraction. *Phys. B Condens. Matter* **1993**, *192*, 55–69.
- (58) FullProf Suite.
- (59) Briois, V.; La Fontaine, C.; Belin, S.; Barthe, L.; Moreno, T.; Pinty, V.; Carcy, A.; Girardot, R.; Fonda, E. ROCK : the new Quick-EXAFS beamline at SOLEIL. *J. Phys. Conf. Ser.* **2016**, *712*, 012149.
- (60) Ravel, B.; Newville, M. ATHENA, ARTEMIS, HEPHAESTUS: data analysis for X-ray absorption spectroscopy using IFEFFIT. *J. Synchrotron Radiat.* **2005**, *12*, 537–541.
- (61) Kresse, G.; Furthmüller, J. Efficiency of ab-initio total energy calculations for metals and semiconductors using a plane-wave basis set. *Comput. Mater. Sci.* **1996**, *6*, 15–50.
- (62) Kresse, G.; Furthmüller, J. Efficient iterative schemes for ab initio total-energy calculations using a plane-wave basis set. *Phys. Rev. B - Condens. Matter Mater. Phys.* **1996**, *54*, 11169–11186.

- (63) Perdew, J.; Burke, K.; Ernzerhof, M. Generalized Gradient Approximation Made Simple. *Phys. Rev. Lett.* **1996**, *77*, 3865–3868.
- (64) Dudarev, S. L.; Botton, G. a.; Savrasov, S. Y.; Humphreys, C. J.; Sutton, A. P. Electron-energy-loss spectra and the structural stability of nickel oxide: An LSDA+U study. *Phys. Rev. B* **1998**, *57*, 1505–1509.
- (65) Parr, R. G.; Yang, W. T. Density functional approach to the frontier-electron theory of chemical reactivity. *J. Am. Chem. Soc.* **1984**, *106*, 4049–4050.

TOC

